

Gas Damping Effect on Thin Vibrating Gold Plates: Experiments and Modeling

G. De Pasquale¹, T. Veijola², A. Somà¹¹ Mechanical Department, Politecnico di Torino, Corso Duca degli Abruzzi 24, 10129 Torino (Italy)² Helsinki University of Technology, P.O. Box 3000, FIN-02015 TKK (Finland)

e-mail: giorgio.depasquale@polito.it, timo.veijola@tkk.fi, aurelio.soma@polito.it

Abstract – Dynamic behavior of oscillating perforated gold plates under the effect of squeeze film damping is analyzed by means of experimental measurements and a compact model. Thin plates built with the surface micro-machining technique and gold electroplating were designed with many different geometrical dimensions for the plate and the holes; the number of holes is also variable. Altogether, samples with 28 square and 6 rectangular plate topologies were fabricated and measured. The quality factors of the fundamental oscillation modes have been extracted from the measurements through the half-power method and compared with a compact model of perforated dampers. The comparison results show that the gas damping model alone is not sufficient in modeling the damping in gold structures. One of the reasons is that the material damping of gold increases the measured damping coefficient.

I. INTRODUCTION

Micro Electro Mechanical Systems (MEMS) are characterized by many different features and shapes and contain numerous oscillating elements and components. Although the structural parts greatly differ between applications, oscillating elements derived from the classical beam or plate shape are largely widespread. Perforations are used in micromechanical squeeze-film dampers for several reasons. Plate perforation is often necessary for sacrificial-layer removal during building processes of MEMS devices, representing a technological constraint for the designer. The main purpose is to reduce the damping and spring forces of oscillating structures due to the gas flow in small air gaps inside and around the oscillating structure. The proper characterization of the gas flow is the goal of many experimental and theoretical studies.

Experiments are needed to ensure that all necessary physical phenomena are taken into account in the characterization. The half-power method, one of the most popular methods, is used to extract the quality factor of the resonance. This method uses directly the specification of the quality factor: the resonance frequency and the -3dB frequencies are measured. Experimental strategies for the measurement of dynamic parameters of MEMS dampers and experimental validation of estimated results have been proposed in [1-3].

The main difficulty in the modeling is the correct estimation of pressure distribution inside and below the holes

in the air gap in order to evaluate the damping force acting on the movable 3D structure. Generally, the volume of fluid surrounding the plate should be considered in the analysis, making the 3D analysis very complicated. These are the reasons why reduced-dimension models have been developed. These models enable the simulation of complicated cases, as well as make the computation much faster. There are several works in the literature reporting dimension-reduction numerical models [4-6]; compact analytic models have been also presented in [7-9].

It is well known that the material damping of silicon is very low and silicon MEMS resonators operating in vacuum are able to reach quality factors of tens of thousands. On the other hand, measurements have shown that even a thin gold layer in a silicon cantilever beam will considerably decrease the quality factor [10]. Thus, the quality factors of the gold structures are expected to be limited by the material damping.

In our previous work [3], perforated silicon resonator structures were measured using the optical interferometric technique, and the damping coefficients were compared with those given by four different compact damping models. It turned out that all the models explained the measurements with reasonable accuracy. Also, the study showed that purely viscous models were sufficient (inertia and compressibility were negligible).

This work is also focused in similar comparison, but the structures have been micro-machined of gold. Since the perforated plates are relatively thin (6.3 μm thickness, while the thickness of the silicon structures was 15 μm), it is also necessary to consider the bending of the plates and the contribution of the springs in the damping. Here, a single compact model is used since the previous work did not show large differences between the models.

II. TEST STRUCTURES

Two topologies of specimens are considered in this work: square and rectangular. Both types were built at FBK (Trento, Italy) by means of the surface micro-machining technique and gold electroplating [11]. The first type of specimen is a square plate, which was designed according to the geometry presented in [1] and is shown in figure 1(a). The plate side dimension is variable, as is the holes' side and the number of holes. The nominal thickness of the plate h_c is 6.3 μm and the air gap height h is 3.0 μm . The average

measured dimensions of the supporting beams are $L_B = 96.66\mu\text{m}$ (length), $W_B = 12.88\mu\text{m}$ (width) and $2.606\mu\text{m}$ (thickness) for square structures. Figure 1(b) shows the optical image of one of the dampers.

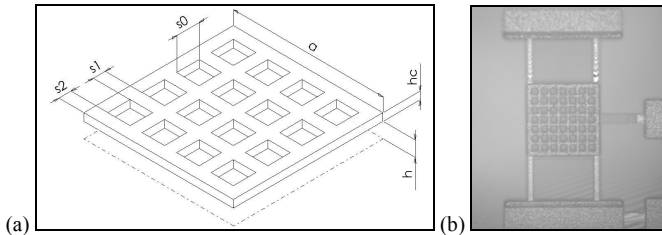


Fig. 1. First topology of specimens: suspended square plates with square holes; (a) drawing of shape characteristics and (b) optical image.

The dimensions of the plates are given in table I, where nominal and measured dimensions of plates and holes are indicated; the total number of holes, $M \times M$, is also reported. The dimensions indicated have been measured by the optical profilometer and they are affected by the sensitivity error given by the microscope resolution ($0.6\mu\text{m}$ horizontal and 0.1nm vertical).

TABLE I
NOMINAL AND MEASURED PLATE DIMENSIONS OF FIRST TYPE OF SPECIMENS
(SQUARE PLATE)

Topol. index	Plate side a [μm]		Holes side s_0 [μm]		Number of holes $M \times M$	Measured plate thickness h_c [μm]
	nom.	meas.	nom.	meas.		
1	55	55.91	7.20	7.20	4	6.297
2		55.07	9.30	9.31		6.291
3		55.70	10.70	10.70		6.302
4		55.89	12.60	12.59		6.322
5	76	76.25	7.20	7.18	9	6.311
6		76.40	9.30	9.29		6.303
7		76.47	10.70	10.68		6.311
8		76.41	12.60	12.62		6.299
9	96	96.45	7.20	7.21	16	6.309
10		96.51	9.30	9.31		6.298
11		96.33	10.70	10.68		6.307
12		96.12	12.60	12.61		6.296
13	115	115.47	7.20	7.21	25	6.304
14		115.42	9.30	9.31		6.275
15		115.39	10.70	10.71		6.298
16		115.74	12.60	12.60		6.302
17	137	137.14	7.20	7.21	36	6.307
18		137.08	9.30	9.31		6.296
19		137.13	10.70	10.68		6.332
20		137.11	12.60	12.61		6.286
21	157	157.31	7.20	7.18	49	6.303
22		157.28	9.30	9.29		6.278
23		157.63	10.70	10.69		6.285
24		157.13	12.60	12.59		6.285
25	185	185.96	7.20	7.19	64	6.312
26		185.28	9.30	9.33		6.321
27		185.97	10.70	10.70		6.287
28		185.13	12.60	12.58		6.297

The values of s_1 and s_2 , indicated in figure 1(a), can be calculated with the following relations:

$$s_1 = \frac{a}{M+1} - s_0 \quad (1)$$

$$s_2 = \frac{a}{M+1} - \frac{s_0}{2} \quad (2)$$

The specimens of the second type of are characterized by different plate lengths and widths; these dampers were also built with the same process used for the first topology. The shape of this second group was presented by the authors in [12] when polysilicon plates were studied; the shape was preserved except for the plate thickness which is lower for new structures. Figure 2 shows a drawing of the device's shape and figure 3 illustrates the difference between one current (thin gold) specimen and one previous (thick silicon) specimen.

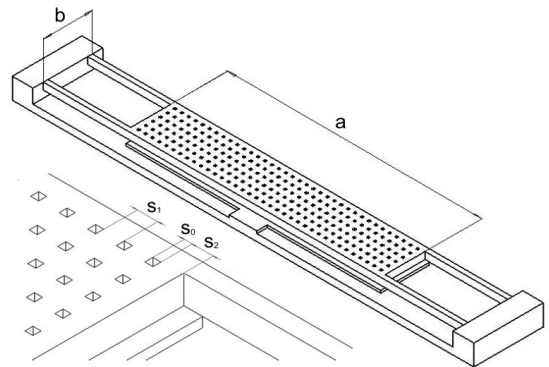


Fig. 2. Second type of specimens: rectangular plates with square holes.

The values of s_1 and s_2 , indicated in figure 2, can be calculated with the same relations as eqs. (1) and (2) or with the following, written for the short side of the plate:

$$s_1 = \frac{b}{N+1} - s_0 \quad (3)$$

$$s_2 = \frac{b}{N+1} - \frac{s_0}{2} \quad (4)$$

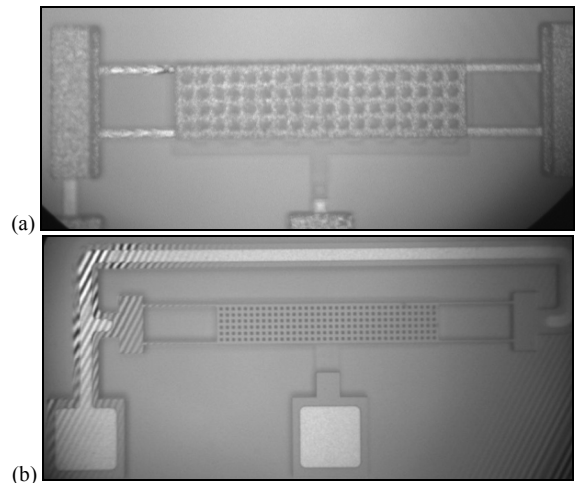


Fig. 3. Second topology of specimens: (a) measured gold plates and (b) previously studied polysilicon plates.

Despite the similarities in structure shapes of the gold and the silicon sets, there are some differences in geometrical dimensions. These are caused by different dimensional

tolerances and design rules of the different building techniques used. The geometrical parameters of the gold specimens are listed in table II; the number of holes present on the longer (M) and shorter (N) side of the plate are indicated. The average measured dimensions of the supporting beams for rectangular gold structures are $L_B = 96.08\mu\text{m}$ (length), $W_B = 13.52\mu\text{m}$ (width) and $2.620\mu\text{m}$ (thickness).

TABLE II
NOMINAL AND MEASURED PLATE DIMENSIONS OF SECOND TYPE OF SPECIMENS (RECTANGULAR PLATE)

Topol. index	Plate length a [μm]		Plate width b [μm]		Holes side s_0 [μm]		Number of holes $M \times N$	Meas. plate thickness h_e [μm]
	nom.	meas.	nom.	meas.	nom.	meas.		
	29	376.13		96.66	7.20	7.21		
30	376.47		96.50	9.30	9.29	18x4	6.303	
31	376.81		96.63	10.70	10.69	18x4	6.257	
32	376.47		96.61	12.60	12.60	18x4	6.323	
33	376.44	158	156.94	7.20	7.21	18x7	6.302	
34	376.13	277	276.98	7.20	7.20	18x13	6.312	

III. EXPERIMENTAL SETUP

The experiments were performed with the optical interferometric microscope ZoomSurf3D, Fogale Nanotech [13]. The suspended plates were excited using a DC voltage generator and AC actuation. The frequency response function (FRF) of the device is measured by means of a sine sweep procedure in order to detect the structural resonance. The microscope can perform profile measurements from a minimum area of $100 \times 100 \mu\text{m}^2$ to a maximum of $2 \times 2 \text{mm}^2$. The actual setting provides a 20x objective magnification factor that reaches a $0.6\mu\text{m}$ and a 0.1nm lateral and vertical resolutions, respectively. A single measurement can detect a $400\mu\text{m}$ maximum difference in height. Light radiation is emitted by a selectable source (continuous or stroboscopic, monochromatic or polychromatic), then exploited to optical interference phenomena generation and spatial reconstruction of specimen. The instrument is equipped with a 3-axis movable piezo-electrical stage and a voltage generator (0-200V, up to 2MHz).

IV. TESTING PROCEDURE

The *half-power method* has been used to extract damping and stiffness parameters of the vibrating system. The area considered for the measurement of the oscillation amplitude is situated in a square region at the center of the plate; the order of magnitude of the average oscillation amplitudes at resonance is $0.1\mu\text{m}$. The experimental FRF is considered only in a small range around the resonance frequency, obtaining a relation between the amplitude of oscillation and the actuation frequency; this relation is composed of a series of discrete values which have been stored in correspondence to many frequency steps. This empirical curve is then interpolated by means of the polynomial function $h(f)$, and the absolute maximum of the interpolated function is then calculated, corresponding to the maximum of FRF. The value of the FRF, which corresponds to the half-power level (3dB lower than the peak), is then calculated as

$$[h(f)]_{-3\text{dB}} = \frac{\max[h(f)]}{\sqrt{2}} \quad (5)$$

and two half-power points are extracted at the frequencies f^I and f^{II} , respectively:

$$[h(f)]_{-3\text{dB}} = h(f^I) \quad (6)$$

$$[h(f)]_{-3\text{dB}} = h(f^{II}) \quad (7)$$

The *half-power bandwidth* is then given by

$$\Delta f = f^{II} - f^I = 2\zeta f_n \quad (8)$$

The resonance frequency of the system f_n is measured experimentally, allowing the use of equation (8) for the extraction of the damping ratio ζ . The damping (c_m) and spring (k_m) coefficients can be calculated using equations (9) and (10) below by means of the modal mass m_m . The exact value of the modal mass involved in the resonance mode studied can be estimated using a finite element method (FEM) numerical model.

$$c_m = 2m_m\zeta(2\pi f_n) \quad (9)$$

$$k_m = m_m(2\pi f_n)^2 \quad (10)$$

V. MODELING

A characterization of the flow problem is needed before any model calculations of estimated damping coefficients and quality factors. The following issues should be considered: flow patterns, gas rarefaction, and contribution of compressibility and inertia.

The flow pattern study can be performed by comparing the damping in two cases: the closed holes case and the closed borders case. If the study shows that one flow pattern dominates, the second pattern can be neglected from the analysis. The flow pattern can be characterized simply with the perforation ratio, which is the ratio between the perforated area and the area of the rigid, unperforated plate. Here, the perforation ratios vary a lot, indicating that the simpler "closed borders" case is not sufficient.

The gas rarefaction becomes very important if the flow channels are narrow. The channel dimensions and atmospheric air pressure conditions indicate that the flow is in the slip flow regime, and simple flow rate coefficients are valid for the estimation of the contribution of the rarefied gas effects. For minimum gap height and hole dimension, the flow rate coefficients are $Q_{\text{ch}} = 1 + 6K_{\text{ch}} = 1.13$ and $Q_{\text{tb}} = 1 + 4K_{\text{tb}} = 1.07$, where $K_{\text{ch}} = \lambda/h$ and $K_{\text{tb}} = \lambda/r = \lambda/(7.2\mu\text{m}/2)$, respectively. The mean free path of air in atmospheric pressure, $\lambda = 65\text{nm}$, is used here. The rarefied gas effects will decrease the damping coefficient by about 10%.

The compressibility changes the quality factor of the resonators in two ways. First, the damping coefficient c is a frequency dependent function of viscous and compressible gas forces. Second, the compressibility of the gas introduces spring forces, in addition to the mechanical spring forces due to the resonator supports and bending of the plate. According to the mass-spring system model, the quality factor is $Q = (k_e m_e)^{1/2}/c$, where k_e is the effective spring coefficient containing the mechanical and gas spring components, and m_e is the effective mass. The contribution of the compressibility

to the damping coefficient c can be estimated with the squeeze number

$$\sigma = \frac{12\mu L^2 \omega}{p_0 h^2} \quad (11)$$

where μ is the viscosity coefficient of air ($18.5 \cdot 10^{-6}$ Ns/m²), L is the characteristic length of the structure and p_0 is the static pressure. In perforated structures the characteristic dimension is the smallest dimension, in practice, the interspace (e.g., s_1 in figs. 1(a) and 2). If $\sigma \ll 1$, the compressibility need not to be considered in the analysis. In the measured structures, the largest characteristic length that gives the largest squeeze number of 0.0078 at frequency 60kHz, is $L = 10\mu\text{m}$.

The inertia of the gas is dependent on the characteristic radius r of the perforation and the density ρ of the gas. The measure for the inertia effect in channel flows is the Reynolds number $Re = \rho r^2 \omega / \mu$. Here, the characteristic radius of the largest aperture ($12.6 \mu\text{m}/2$) gives $Re = 1.0$ at 60kHz.

It is evident that the "viscous" low-frequency model is applicable also here. From our previous work [3], we select here model M3 [9]. Model equations are presented in the appendix, with the damping coefficient c in Eq (A1). The contribution of the gas damping of the springs is also included with an approximate equation. The lengths of the springs are much larger than their widths, justifying the use of a 1-dimensional damping model. For translational motion and without the border and rarefaction effects the damping coefficient is $c = L_b W_b^3 \mu / h^3$ for each spring. Considering four springs, non-translational motion, border elongations, and slip conditions, the estimated damping coefficient due to the springs is

$$c_b = \frac{4 L_b (W_b + 1.3h)^3 \mu}{2 h^3 (1 + 6K_{ch})} \quad (12)$$

VI. RESULTS

Some experimental FRF are presented in figure 4 as an example. Measured values of resonance frequency, half-power bandwidth, damping coefficients and quality factors are listed in tables III and IV for the two topologies of test structures, respectively. The ratio between modal mass and total mass is also indicated for each specimen. The modal mass has been calculated with FEM analysis (figure 5).

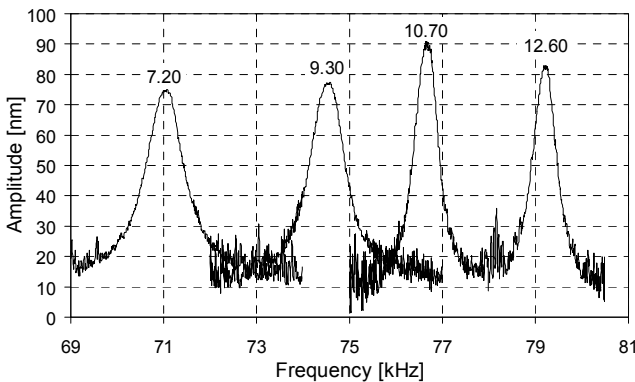


Fig. 4. Experimental FRF for square dampers with 55µm nominal plate side and various holes sides (indicated above each curve).

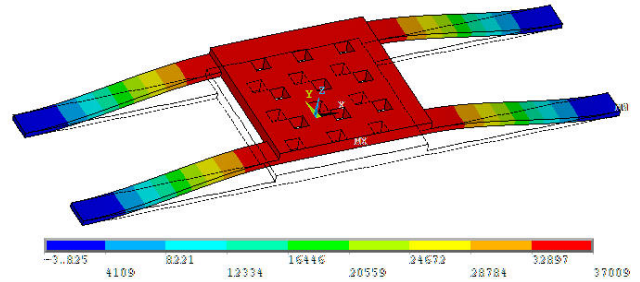


Fig. 5. FEM modal deformed shape of one gold damper (topology index 5).

TABLE III
EXPERIMENTAL RESULTS OF FIRST DAMPERS TOPOLOGY (SQUARE)

Topol. index	Resonance frequency f_n [kHz]	Half-power bandwidth Δf [kHz]	Mass ratio	Damping coefficient c_m [Ns 10^{-6} /m]	Q-factor
1	71.04	0.7389	0.8515	2.341	96.14
2	74.54	0.7143	0.8456	2.124	104.35
3	76.67	0.4998	0.8402	1.492	153.40
4	79.21	0.3984	0.8301	1.168	198.82
5	58.16	0.6172	0.8939	3.143	94.23
6	59.65	0.6103	0.8893	2.970	97.74
7	61.57	0.5264	0.8831	2.483	116.96
8	63.58	0.3888	0.8764	1.702	163.52
9	47.78	0.8296	0.9229	6.218	57.59
10	48.76	0.6486	0.9180	4.588	75.18
11	50.69	0.5260	0.9129	3.542	96.37
12	54.06	0.5487	0.9044	3.374	98.52
13	41.27	0.8823	0.9403	9.030	46.77
14	42.28	0.6353	0.9362	6.043	71.27
15	43.80	0.5170	0.9326	5.155	84.72
16	45.66	0.5607	0.9269	4.606	81.43
17	34.17	0.7733	0.9561	10.796	44.19
18	35.03	0.5770	0.9527	7.478	60.71
19	36.61	0.5239	0.9501	6.433	69.88
20	39.72	0.5541	0.9423	6.087	71.68
21	29.82	0.8886	0.9660	15.966	33.56
22	29.86	0.6305	0.9636	10.450	47.36
23	31.00	0.5939	0.9604	9.292	52.20
24	33.60	0.5833	0.9536	8.108	57.60
25	22.04	0.7785	0.9773	19.334	28.31
26	25.36	0.5913	0.9729	13.611	42.89
27	26.28	0.5592	0.9709	12.163	47.00
28	28.13	0.5584	0.9660	10.843	50.38

TABLE IV
EXPERIMENTAL RESULTS OF SECOND DAMPERS TOPOLOGY (RECTANGULAR)

Topol. index	Resonance frequency f_n [kHz]	Half-power bandwidth Δf [kHz]	Mass ratio	Damping coefficient c_m [Ns 10^{-6} /m]	Q-factor
29	20.25	1.1278	0.9578	28.678	17.95
30	20.70	0.8652	0.9514	20.023	23.92
31	20.98	0.5022	0.9438	10.949	41.78
32	21.92	0.3847	0.9342	7.507	56.98
33	17.00	1.2793	0.9763	52.135	13.29
34	13.61	2.3788	0.9870	169.515	5.72

Figure 6 compares the measured resonant frequencies for the square dampers with those predicted with the FEM simulation. As the figure shows, FEM results are very close to measured values.

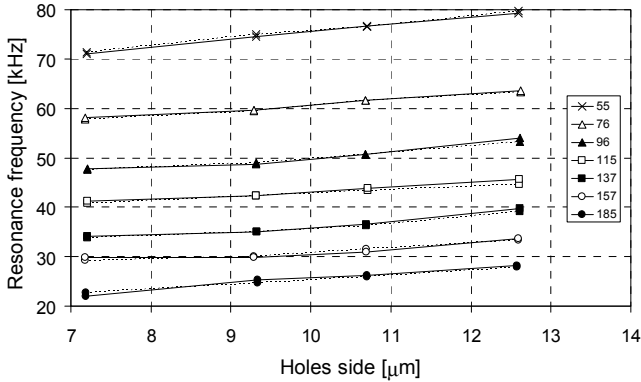


Fig. 6. Experimental (continuous) and numerical (dashed) resonance frequencies of square dampers with different holes sides.

Figure 7 shows the measured damping coefficients together with the results of the gas-damping model (thick black line) for all dampers as a function of the topology index given in tables I and II. Figure 8 shows the relative errors of the simulated damping coefficients.

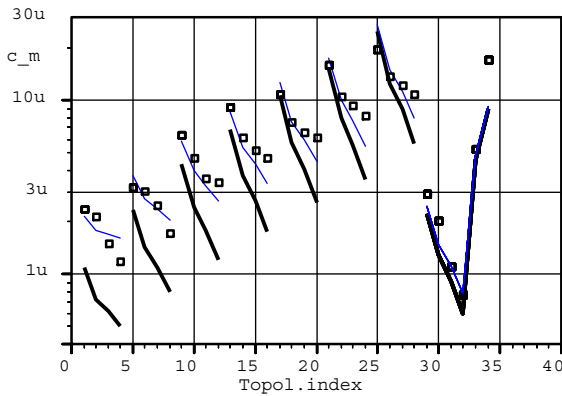


Fig. 7. Experimental damping coefficient (\square) and results of the compact model (thick black line) of all measured dampers (square plates 1-28 c_m , rectangular plates 29-34 $c_m/10$). The thin blue line illustrates the effect of an additional loss mechanism with a constant quality factor of 250.

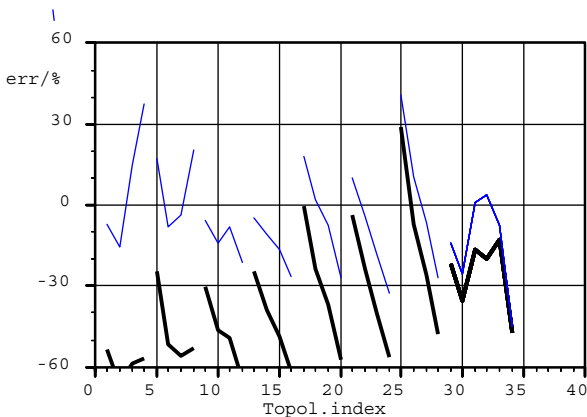


Fig. 8. Relative errors of damping coefficients predicted by the model compared to the measured values and results of the compact model (thick black line). The thin blue line illustrates the relative error in case of additional losses ($Q_{mat} = 250$).

The damping coefficients given by the model are systematically lower than the measured values (except

measurement 25). For each geometry, when the holes become larger, the drop of the damping coefficients predicted by the model are larger with respect to the values measured. This indicates that some other phenomenon is limiting the high Q-values. This is illustrated in Fig. 7 with the thin blue line: an arbitrary additional loss mechanism of a quality factor of $Q_{mat} = 250$ has been included in the damping model. The loss mechanism could be due to the material damping of gold. In spite of additional losses, the drop of the damping coefficient as a function of the hole size is significant. This is probably due to a constant Q_{mat} , that does not take into account increased losses due to the less stiff plate (additional material losses) when the holes are large (the relative bending of the plate is 12.6% for 12.6 μ m holes and 5.5% for 7.2 μ m holes).

VII. CONCLUSIONS

Measured damping coefficients of resonating gold structures could not be explained with a gas damping model alone. It is evident that the material losses of gold contribute here, making the measured damping coefficients larger than the predicted ones. To be able to extract the material damping coefficients, measurements in vacuum should be performed. We were not able to study the contribution of the springs to the damping force, nor the change in the mass ratio due to the mass of the springs.

Since the quality factors are relatively low for small holes, the damping forces may change the mode shapes from the ones that have been analyzed here. Moreover, for small holes the "the closed holes" flow pattern is strong. In this case the damping pressure concentrates in the centre of the plate and reduces the bending of the plate.

REFERENCES

- [1] G. De Pasquale and T. Veijola, "Comparative numerical study of FEM methods solving gas damping in perforated MEMS devices," *Microfluidics and Nanofluidics*, vol. 5 (4), pp. 517-528, 2008.
- [2] G. De Pasquale and A. Somà, "Energetic method for non linear dynamic characterization of MEMS squeeze film damping," *proc. ECCOMAS 2008*, Venice, Italy, 2008.
- [3] T. Veijola, G. De Pasquale and A. Somà, "Comparison Between Damping Coefficients of Measured Perforated Structures and Compact Models," *proc. Symposium on Design, Test, Integration and Packaging of MEMS/MOEMS (DTIP)*, pp. 236-241, Nice, France, 2008.
- [4] J.B. Starr, "Squeeze-film Damping in Solid State Accelerometers," *IEEE Solid-State Sensor and Actuator Workshop*, pp. 44-47, Hilton Head Island, 1990.
- [5] R. Sattler and G. Wachutka, "Analytical Compact Models for Squeezed-Film Damping," *proc. Symposium on Design, Test, Integration and Packaging of MEMS/MOEMS (DTIP)*, pp. 377-382, Montreux, 2004.
- [6] T. Veijola, "Methods for Solving Gas Damping Problems in Perforated Microstructures Using a 2D Finite-Element Solver," *Sensors*, vol. 7, pp. 1069-1090, 2007.
- [7] M. Bao, H. Yang, Y. Sun and P.J. French, "Modified Reynolds' equation and analytical analysis of perforated structures," *J Micromech Microeng.*, vol. 13, pp. 795-800, 2003.
- [8] S.S. Mohite, H. Kesari, V.R. Sonti and R. Pratap, "Analytical solutions for the stiffness and damping coefficients of squeeze films in MEMS devices with perforated back plates," *J Micromech Microeng.*, vol. 15, pp. 2083-2092, 2005.

- [9] T. Veijola, "Analytic Damping Model for an MEM Perforation Cell," *Microfluidics and Nanofluidics*, vol. 2, pp. 249-260, 2006.
- [10] R. Sandberg, K. Mølhave, A. Boisen and W. Svendsen, "Effect of gold coating on the Q-factor of a resonant cantilever," *J Micromech Microeng*, vol. 15, pp. 2249-2253, 2005.
- [11] B. Margesin, A. Bagolini, I. Guamieri, F. Giacomozzi and A. Faes, "Stress characterization of electroplated gold layers for low temperature surface micromachining," *proc. Symposium on Design, Test, Integration and Packaging of MEMS/MOEMS (DTIP)*, Mandelieu, France, 2003.
- [12] A. Somà and G. De Pasquale, "Numerical and experimental comparison of MEMS suspended plates dynamic behaviour under squeeze film damping effect," *Analog Integrated Circ S*, vol. 57, pp. 213-224, 2008.
- [13] Fogale Nanotech: <http://www.fogale.fr>.

Appendix: Damping model

A model for a circular perforation cell is derived in [9], and the damping coefficient of a rectangular perforated plate is given in the paper.

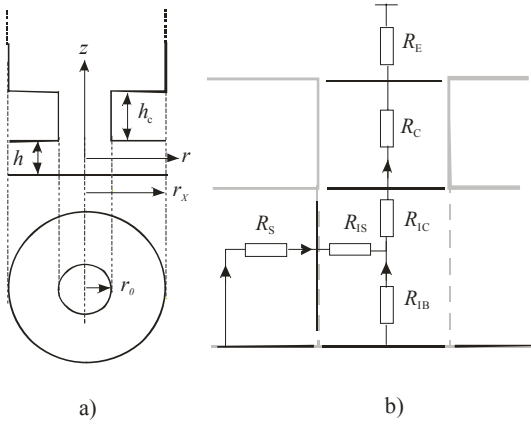


Fig. 9. a) Structure of a perforation cell with a circular hole and b) the lumped flow resistances.

The damping coefficient c is

$$c = \sum_{m=1,3,5,\dots}^{\infty} \sum_{n=1,3,5,\dots}^{\infty} \frac{1}{G_{m,n}(a_{\text{eff}}, b_{\text{eff}}) + 1/R_{m,n}} \quad (\text{A1})$$

where the effective surface dimensions are

$$a_{\text{eff}} = a + 1.3(1 + 3.3K_{\text{ch}})h$$

$$b_{\text{eff}} = b + 1.3(1 + 3.3K_{\text{ch}})h$$

and

$$G_{m,n}(a, b) = \left(\frac{m^2}{a^2} + \frac{n^2}{b^2} \right) \frac{m^2 n^2 \pi^6 h^3 Q_{\text{ch}}}{768 \mu a b}$$

$$R_{m,n} = \frac{64 M N R_p}{m^2 n^2 \pi^4}$$

The flow resistance of a single perforation cell is

$$R_p = R_S + R_{IS} + R_{IB} + \frac{r_X^4}{r_0^4} (R_{IC} + R_C + R_E)$$

where

$$R_S = \frac{12 \pi \mu r_X^4}{Q_{\text{ch}} h^3} \left(\frac{1}{2} \ln \frac{r_X}{r_0} - \frac{3}{8} + \frac{r_0^2}{2 r_X^2} - \frac{r_0^4}{8 r_X^4} \right)$$

$$R_{IS} = \frac{6 \pi \mu (r_X^2 - r_0^2)^2}{r_0 h^2} \Delta_S$$

$$R_{IB} = 8 \pi \mu r_0 \Delta_B$$

$$R_{IC} = 8 \pi \mu r_0 \Delta_C$$

$$R_C + R_E = 8 \pi \mu \left(\frac{h_C}{Q_{\text{tb}}} + \Delta_E r_0 \right)$$

where the equivalent radii of the circular perforation cell and the hole are

$$r_x = \frac{s_0 + s_1}{\sqrt{\pi}}$$

$$r_0 = \frac{1.096 s_0}{2} \approx 0.547 s_0$$

respectively, and the elongations are

$$\Delta_S = \frac{0.56 - 0.32 \frac{r_0}{r_X} + 0.86 \frac{r_0^2}{r_X^2}}{1 + 2.5 K_{\text{ch}}}$$

$$\Delta_B = 1.33 \left(1 - 0.812 \frac{r_0^2}{r_X^2} \right) \frac{1 + 0.732 K_{\text{tb}}}{1 + K_{\text{ch}}} f_B \left(\frac{r_0}{h}, \frac{h_C}{h} \right)$$

$$\Delta_C = (1 + 6 K_{\text{tb}}) \left(0.66 - 0.41 \frac{r_0}{r_X} - 0.25 \frac{r_0^2}{r_X^2} \right)$$

$$\Delta_E = \frac{0.944 \cdot 3\pi (1 + 0.216 K_{\text{tb}})}{16} \times$$

$$\left(1 + 0.2 \frac{r_0^2}{r_X^2} - 0.754 \frac{r_0^4}{r_X^4} \right) f_E \left(\frac{r_0}{h} \right)$$

where the functions are

$$f_B(x, y) = 1 + \frac{x^4 y^3}{7.11(43y^3 + 1)}$$

$$f_E(x) = 1 + \frac{x^{3.5}}{178(1 + 17.5 K_{\text{ch}})}$$

The flow rate coefficients and Knudsen numbers for the air gap and the holes are

$$Q_{\text{ch}} = 1 + 6 K_{\text{ch}}, \quad K_{\text{ch}} = \frac{\lambda}{h}$$

$$Q_{\text{tb}} = 1 + 4 K_{\text{tb}}, \quad K_{\text{tb}} = \frac{\lambda}{r_0}$$